Atmospheric
Chemistry
and Physics

Effects of OH radical and SO_2 concentrations on photochemical reactions of mixed anthropogenic organic gases

Junling Li[1], **Kun Li**[2,3], **Hao Zhang**[1], **Xin Zhang**[1], **Yuanyuan Ji**[1], **Wanghui Chu**[1], **Yuxue Kong**[1], **Yangxi Chu**[1], **Yanqin Ren**[1], **Yujie Zhang**[1], **Haijie Zhang**[1], **Rui Gao**[1], **Zhenhai Wu**[1], **Fang Bi**[1], **Xuan Chen**[1], **Xuezhong Wang**[1], **Weigang Wang**[4], **Hong Li**[1], and **Maofa Ge**[4]

[1]State Key Laboratory of Environmental Criteria and Risk Assessment, Chinese Research Academy of Environmental Sciences, Beijing 100012, China
[2]Laboratory of Atmospheric Chemistry, Paul Scherrer Institute, 5232 Villigen, Switzerland
[3]Environment Research Institute, Shandong University, Qingdao 266237, China
[4]State Key Laboratory for Structural Chemistry of Unstable and Stable Species Beijing National Laboratory for Molecular Sciences (BNLMS), CAS Research/Education Center for Excellence in Molecular Sciences, Institute of Chemistry, Chinese Academy of Sciences, Beijing 100190, China

Correspondence: Hong Li (lihong@craes.org.cn) and Maofa Ge (gemaofa@iccas.ac.cn)

Abstract. Vehicle exhaust, as a major source of air pollutants in urban areas, contains a complex mixture of organic vapours including long-chain alkanes and aromatic hydrocarbons. The atmospheric oxidation of vehicle emissions is a highly complex system as inorganic gases (e.g. NO_x and SO_2) from other urban sources coexist and therefore remains poorly understood. In this work, the photooxidation of n-dodecane, 1,3,5-trimethylbenzene, and their mixture is studied in the presence of NO_x and SO_2 to mimic the atmospheric oxidation of urban vehicle emissions (including diesel and gasoline vehicles), and the formation of ozone and secondary aerosols is investigated. It is found that ozone formation is enhanced by higher OH concentration and higher temperature, but is influenced little by SO_2 concentration. However, SO_2 can largely enhance the particle formation in both number and mass concentrations, likely due to the promoted new particle formation and acid-catalysed heterogeneous reactions from the formation of sulfuric acid. In addition, organo-sulfates and organo-nitrates are detected in the formed particles, and the presence of SO_2 can promote the formation of organo-sulfates. These results provide a scientific basis for systematically evaluating the effects of SO_2, OH concentration, and temperature on the oxidation of mixed organic gases in the atmosphere that produce ozone and secondary particles.

1 Introduction

Atmospheric fine particulate matter with diameters $< 2.5\,\mu m$ ($PM_{2.5}$) is a common air pollutant that has a variety of adverse health outcomes (Requia et al., 2018; Tsai et al., 2013; Crouse et al., 2012). Organic aerosol (OA) is an important type of $PM_{2.5}$, and secondary organic aerosol (SOA) accounts for more than 50 % of OA by mass concentration (Guo et al., 2010; R. J. Huang et al., 2014;

Jimenez et al., 2009; Kanakidou et al., 2005). In China, concentrations of $PM_{2.5}$ have declined with the implementation of stringent emission control measures since 2013 (Gao et al., 2020; Zhang et al., 2019; Cheng et al., 2019). The level of primary organic aerosol (POA) in $PM_{2.5}$ has been greatly reduced; however, the contribution of SOA to $PM_{2.5}$ has increased (Ming et al., 2017), highlighting the increasing importance of research on SOA.

Intermediate volatile organic compounds (IVOCs) have been found to contribute to a large fraction of SOA in both field observations (Fang et al., 2021; C. Wang et al., 2020; Xu et al., 2020) and laboratory studies (Srivastava et al., 2022; Hu et al., 2021; Cai et al., 2019; Li et al., 2019a, b). Laboratory studies of long-chain alkanes, as representatives of IVOCs, are mainly focused on the case of a single long-chain alkane or mixture of various precursors which include long-chain alkanes. Studies of single long-chain alkanes (e.g. *n*-decane, *n*-undecane, *n*-dodecane, *n*-tridecane, 2,6,10-trimethyl dodecane, nonyl-cyclohexane) include reaction kinetics (Lamkaddam et al., 2019; Shi et al., 2019a, b), reaction mechanisms (Li et al., 2020, 2021a; J. Li et al., 2017), analysis of gas phase and particle phase products (Fahnestock et al., 2015; Lamkaddam et al., 2020), quantification of particle yield (Docherty et al., 2021; Loza et al., 2014), and particle physicochemical properties (J. Li et al., 2017; Li et al., 2020, 2021a). For the mixture of various precursors including long-chain alkanes, studies are mainly focused on the chemical composition of the mixture gases, the properties of total organic carbon, the amount of SOA generated, and the effect of semi-volatile and intermediate-volatility organic compounds (S/IVOCs) on the formation of SOA contribution (Qi et al., 2019, 2021; Hu et al., 2021; Cai et al., 2019; Deng et al., 2017; K. Li et al., 2019a, b, 2021). However, laboratory studies on the mixture of long-chain alkanes and aromatic hydrocarbons (e.g. 1,3,5-trimethylbenzene, *m*-xylene, benzene, toluene, ethylbenzene) are very limited (Li et al., 2021b), despite both of them being important SOA precursors in vehicle exhaust emissions (Qi et al., 2021).

As an important chemical component of inorganic pollutants in China, SO₂ has a high concentration in the urban atmosphere (Chu et al., 2016; Liu et al., 2016, 2017; Wang et al., 2019). Field observations in North China Plain showed that during heavy-haze-pollution episodes, SO₂ concentration could be > 100 ppb, and the formation and growth rates of SOA and sulfate were much faster than that during clean periods (H. Li et al., 2017). Laboratory studies demonstrated that the presence of SO₂ could enhance the SOA formation from anthropogenic and biogenic precursors, e.g. monoterpenes, isoprene, aromatics (Liggio and Li, 2013; Santiago et al., 2012; Kleindienst et al., 2006; Zhang et al., 2020; Yang et al., 2020; Liu et al., 2019). In addition, the presence of SO₂ could affect the light scattering and absorption properties of formed SOA (Zhang et al., 2020; Jaoui et al., 2008; Nakayama et al., 2015, 2018). It should be noted that most of the previous studies focused on the effect of SO₂ on the particle formation from a single precursor. However, the studies on the impact of SO₂ on particle formation in mixture systems are very limited, although it has important atmospheric implications in better understanding the complex chemical processes in urban areas.

According to the field observation in China, higher concentrations of 1,3,5-TMB and *n*-dodecane were observed. The 1,3,5-TMB concentration at a rural site could reach 1447 ppb, and the measured concentration of C₁₂ alkanes at a rural site was 0.122±0.12 ppb (T. Chen et al., 2020; C. Wang et al., 2020). In addition, the content of 1,3,5-TMB and *n*-dodecane in liquid gasoline cannot be ignored (Schauer et al., 2002; Gentner et al., 2012). In this work, a large outdoor smog chamber was used to investigate the effects of SO₂ on particle formation from the mixture of *n*-dodecane and 1,3,5-trimethylbenzene (1,3,5-TMB) in the presence of NO$_x$. Ozone and particle formation were analysed. The results in this work are helpful to improve our understanding of the effect of inorganic gases on anthropogenic mixture organic compounds.

2 Experimental section

2.1 Smog chamber experimental conditions

The experiments were performed in a 56 m³ outdoor smog chamber, which was built on the rooftop of a building located at Chinese Research Academy Environmental Sciences (CRAES). The details of the chamber have been described elsewhere (Li et al., 2021c). Briefly, fluorinated ethylene propylene Teflon film (FEP 100, DuPont USA) was used as the reactor wall. Sunlight was the natural light source, and a J_{NO_2} filter radiometer (Metcon, Germany) was used to detect the irradiation intensity inside the chamber. The variation in temperature (T) and relative humidity (RH) inside the chamber was detected by a temperature and humidity sensor (Beijing Star Sensor Technology Co., Ltd.). Three fans were located on the opposite corner of the bottom of the chamber, which were used to mix the gas compounds and seed particles sufficiently. Before each experiment, the chamber was flushed with zero air for at least 24 h with a flow rate of 200 L min⁻¹. A schematic of the experimental setup is shown in Fig. S1 in the Supplement.

All the experiments in this work were performed in winter, of which the initial conditions and results were summarised in Tables S1 and S2 in the Supplement. The entire photochemical reaction process for the conducted experiments lasted 7 h; the enclosure was opened between 09:00–10:00 LT in the morning and closed at 16:30–17:30 LT in the afternoon. Temperature inside the chamber at noon was around 15–30°. As the bottom of the reactor was made of aluminium, after a period of sunlight exposure, the surface temperature of the aluminium plate will rise. The chamber covered by Teflon film is equivalent to a greenhouse; the internal temperature will rise after sunlight exposure. The cooling system of the chamber is water-cooled, and in order to prevent the cooling pipes from being frozen and cracked, the system is closed. Thus, the temperature inside the chamber during winter is higher than in the ambient environment. The relative humidity during the whole photochemical process was < 15 %.

The gas-phase *n*-dodecane and/or 1,3,5-TMB was introduced into the chamber by zero air with a known volume of

liquid *n*-dodecane and/or 1,3,5-TMB, and the injector was heated gently during the sample injection process. NO$_x$ was used as the OH precursor; therefore, NO and HONO experiments were designed, as their pathways for generating OH radicals in the atmosphere were different. HONO could directly generate OH radicals by photolysis, while for NO experiments, the generation of OH radical was through recycling via NO$_x$/HO$_x$ chemistry (Ng et al., 2007). For high-NO$_x$ experiments, NO was introduced from a 500 ppm standard gas cylinder (500 ppm NO in nitrogen); for HONO experiments, HONO was prepared by the dropwise addition of 1 mL 5 wt % NaNO$_2$ into 2 mL 30 wt % H$_2$SO$_4$ in a glass bubbler, and the formed NO, NO$_2$, and HONO was flushed into the chamber with zero air. The measured initial NO$_x$ concentration in the chamber was in the range of 315–445 ppb. SO$_2$ was introduced from a 60 ppm standard gas cylinder (600 ppm SO$_2$ in nitrogen). For experiments with low SO$_2$ concentration (L-HONO/NO-experiments), initial SO$_2$ concentration was in the range of 0–9.5 ppb; for experiments with high SO$_2$ concentration (H-HONO/NO-experiments), initial SO$_2$ concentration was in the range of 25.5–106 ppb. When the target species introduced into the chamber were mixed evenly, the enclosure of the chamber was open and the reaction started.

2.2 Online and offline measurements

Gaseous NO$_x$, SO$_2$, and O$_3$ concentrations inside the chamber were monitored in real time by NO$_x$ (EC 9841, Ecotech, Australia), SO$_2$ (EC 9850, Ecotech, Australia), and O$_3$ analysers (EC 9830, Ecotech, Australia). A HONO analyser (Y. Chen et al., 2020) (Beijing Zhichen Technology Co., Ltd.) was used to measure the HONO concentration during the reaction process. Organic precursors in the chamber were collected with the Tenax TA sorbent before and after the photochemical reactions and were then analysed with a thermal desorption–gas chromatography with flame ionisation detection (GC, 8890; TD, UNITY-xr). Since the concentration of organic precursors after the photooxidation was nearly zero, the initial concentrations are shown in Tables S1 and S2 to represent the organic precursors consumed in the reaction.

The formed particles were monitored with a scanning mobility particle sizer (SMPS, model 3080, model 3081, and model 3772, TSI Inc., USA). The particles were also collected with a low-flow sampler (LV 40BW, Sibata Scientific Technology Ltd., Soka, Japan) at a flow rate of 15 L min^{-1} for 20 min with PTFE filters (0.2 µm, 47 mm, Merck Millipore, type FGLP). Then the collected whole PTFE filter was extracted with 5 mL methanol in an ultrasonic bath (KH5200DV, Hechuang Ultrasonic, China) for 30 min. The extracted solutions were analysed with electrospray ionisation quadrupole time-of-flight mass spectrometry (ESI-Q-ToF-MS, Bruker Compact). Positive ion mode was used for the ESI-Q-ToF-MS, and the mass resolution of this instrument was > 20 000. The concentrations of inorganic species in aerosols (sulfate and nitrate) and gases (nitric acid) for mixture experiments in the chamber were measured with a Monitor for AeRosols and Gases in Ambient air (MARGA 2080, Applikon, Metrohm). The attenuated total internal reflection infrared (ATR-IR) analysis was used to measure the potential functional groups in filter extracts; an FTIR spectrometer (Bruker, Tensor 27) equipped with a RT-DLaTGs detector was applied.

2.3 Calculation methods of SOA yields and OH concentration

Details of the calculation methods of wall-loss corrections and secondary aerosol (SA) yields can be referred to in Li et al. (2021b). Briefly, when calculating the SA yields, the organic vapour and aerosol wall-loss corrections were both considered (Zhang et al., 2014). The ratio of average gas–particle partitioning timescale ($\overline{\tau}_{\text{g-p}}$) to the vapour wall-loss timescale ($\overline{\tau}_{\text{g-w}}$) could be used to evaluate the organic vapour wall-loss correction (Chen et al., 2019).

$\overline{\tau}_{\text{g-p}}$ can be expressed as the following equation:

$$\overline{\tau}_{\text{g-p}} = \frac{1}{2\pi \overline{N}_{\text{p}} \overline{D}_{\text{p}} D_{\text{gas}} \overline{F}_{\text{FS}}}, \tag{1}$$

where $\overline{N}_{\text{p}}$ is the average number concentration of the formed particles during the experiment, $\overline{D}_{\text{p}}$ is the number mean diameter of the particles, D_{gas} is the gas-phase diffusivity, and $\overline{F}_{\text{FS}}$ is the Fuchs–Sutugin correction for noncontinuum mass transfer (Seinfeld and Pandis, 2016).

The gas-phase diffusivity D_{gas} can be expressed as the following equation:

$$D_{\text{gas}} = D_{\text{CO}_2} \times \frac{M_{\text{wCO}_2}}{M_{\text{w}}}, \tag{2}$$

where D_{CO_2} was 1.38×10^{-5} m^2 s^{-1}; M_{w} was set to 300 g mol^{-1} here.

The Fuchs–Sutugin correction for noncontinuum mass transfer $\overline{F}_{\text{FS}}$ can be expressed as follows:

$$\overline{F}_{\text{FS}} = \frac{0.75\alpha(1+k_n)}{k_{\text{n}}^2 + k_{\text{n}} + 0.283k_{\text{n}}\alpha + 0.75\alpha}, \tag{3}$$

where α is the mass accommodation coefficient onto particles, and it was set to 0.002 in this work (Zhang et al., 2014).

$$k_n = \frac{\lambda}{R_{\text{p}}} = \frac{6D_{\text{gas}}}{D_{\text{p}}\overline{c}}, \tag{4}$$

where k_{n} is the Knudsen number, R_{p} is the particle radius, and λ is the gas mean free path.

The vapour wall-loss timescale ($\overline{\tau}_{\text{g-p}}$) can be expressed as follows:

$$\overline{\tau}_{\text{g-p}} = \frac{1}{k_{\text{w}}}, \tag{5}$$

$$k_{\text{w}} = \left(\frac{A}{V}\right) \frac{a_{\text{w}} \frac{\overline{c}}{4}}{1.0 + \frac{\pi}{2} \left[\frac{a_w \overline{c}}{4(k_{\text{e}} D_{\text{gas}})^{0.5}}\right]}, \tag{6}$$

where k_{w} is the wall-loss rates of the organic vapour; $\frac{A}{V}$ is the ratio of surface to volume of the chamber, $1.55\,\text{m}^{-1}$ for this chamber; a_{w} is the mass accommodation coefficient of vapour deposition to the wall (10^{-5} was used here) (Zhang et al., 2014); $\overline{c}$ is the root mean square speed of the gas; and k_{e} is the eddy diffusion coefficient, which was set to $0.12\,\text{s}^{-1}$ according to the reported values for a $60\,\text{m}^3$ chamber (Mc-Murry and Grosjean, 1985).

$$\overline{c} = \sqrt{\frac{8RT}{\pi M_{\text{w}}}}, \tag{7}$$

where R is the ideal gas constant (i.e. $8314\,\text{J}\,\text{mol}^{-1}\,\text{K}^{-1}$), T is the temperature, and M_{w} is the molecular weight.

The particle wall loss was corrected based on the size-dependent coefficients from inert particle (ammonium sulfate) wall-loss experiments:

$$k_{\text{dep}}(d) = 6.35 \times 10^{-6} d^{1.56} + \frac{6.38}{d^{0.67}}, \tag{8}$$

where $k_{\text{dep}}(d)$ is the wall-loss coefficient of particles in the diameter d.

In this work, OH was determined by measuring the concentration of tracer by TD-GC during the mixture experiments (Barmet et al., 2012). Changes in the tracer concentration over time can be expressed as

$$\frac{d[\text{tracer}]}{dt} = -k[\text{OH}][\text{tracer}], \tag{9}$$

where k is the rate constant for the reaction of tracer and OH radical. In the case of a constant OH radical concentration level, Eq. (9) can be integrated into Eq. (10):

$$\ln[\text{tracer}]_0 = k[\text{OH}]t + \ln[\text{tracer}]_t. \tag{10}$$

Plotting the natural logarithm (ln) of the tracer versus time (t), the slope that equals to $k[\text{OH}]$ is obtained. Therefore, average OH radical concentration during each period is expressed as

$$[\text{OH}] = \frac{\ln \frac{[\text{tracer}]_0}{[\text{tracer}]_t}}{kt} = \frac{\text{slope}}{k}. \tag{11}$$

In this work, 1,3,5-trimethylbenzene is chosen as the tracer for the mixture experiments, as it reacts mainly with OH and has no interference from other compounds. The rate constants (Atkinson and Arey, 2003) at 298 K for reaction

of 1,3,5-trimethylbenzene with the OH radical is $5.67 \times 10^{-11}\,\text{cm}^3\,\text{molec.}^{-1}\,\text{s}^{-1}$. Then the OH concentration is calculated with Eq. (11). Combined with the sampling frequency, the time resolution for [OH] calculations is about 1–1.5 h.

The corresponding OH exposure is quantified by normalising the 1,3,5-TMB concentration before the sampling period to the 1,3,5-TMB concentration before the next sampling period and applying the known OH + 1,3,5-TMB rate constant (Atkinson and Arey, 2003), as shown in Eq. (12):

$$\text{OH exposure} = \frac{\ln \frac{[1,3,5\text{-TMB}]_0}{[1.3.5\text{-TMB}]_t}}{k_{\text{OH}+1,3,5\text{-TMB}}}. \tag{12}$$

3 Results and discussions

3.1 General results of the experiments

The HONO experiments were conducted as follows: $1,3,5\text{-TMB} + \text{HONO} + \text{SO}_2$ (HONO-TMB), $n\text{-dodecane} + \text{HONO} + \text{SO}_2$ (HONO-Dod), and $1,3,5\text{-TMB} + n\text{-dodecane} + \text{HONO} + \text{SO}_2$ (HONO-Mix). The concentration of organic precursor was 137.9–216.9 ppb for 1,3,5-TMB and 23.2–28.9 ppb for n-dodecane. The measured NO$_x$ concentration applied in HONO experiments was in the range of 315–429 ppb. According to Ng et al. (2007), this method could generate $(6.3\text{–}8.6) \times 10^6\,\text{molec.}\,\text{cm}^{-3}$ OH initially. As shown in Fig. 1a, the concentration of OH radicals generated at the beginning of the experiment is in the range of $(1.03\text{–}1.23) \times 10^7\,\text{molec.}\,\text{cm}^{-3}$, which is slightly higher than that of Ng et al. (2007). The OH exposure was in the range of 3.74×10^{10} to $7.16 \times 10^{10}\,\text{molec.}\,\text{cm}^{-3}\,\text{s}$, as revealed in Fig. 1b, corresponding to 6.9–13.3 simulated hours, assuming a global average OH concentration of $1.5 \times 10^6\,\text{molec.}\,\text{cm}^{-3}$ (Mao et al., 2009). The reaction profiles of the HONO experiments are shown in Fig. S2.

The NO experiments were conducted as follows: $1,3,5\text{-TMB} + \text{NO} + \text{SO}_2$ (NO-TMB), $n\text{-dodecane} + \text{NO} + \text{SO}_2$ (NO-Dod), and $1,3,5\text{-TMB} + n\text{-dodecane} + \text{NO} + \text{SO}_2$ (NO-Mix). The concentration of organic precursor was 177.8–192.4 ppb for 1,3,5-TMB and 23–29.9 ppb for n-dodecane. The initial NO$_x$ concentration in the chamber was in the range of 212–355 ppb, resulting in the estimated OH concentration of $(3.4\text{–}4.9) \times 10^6\,\text{molec.}\,\text{cm}^{-3}$, as shown in Fig. 1. Using the OH concentration above, the calculated photochemical age from these experiments was in the range of 0.9–11.9 h. The reaction profiles of the NO experiments are shown in Fig. S3.
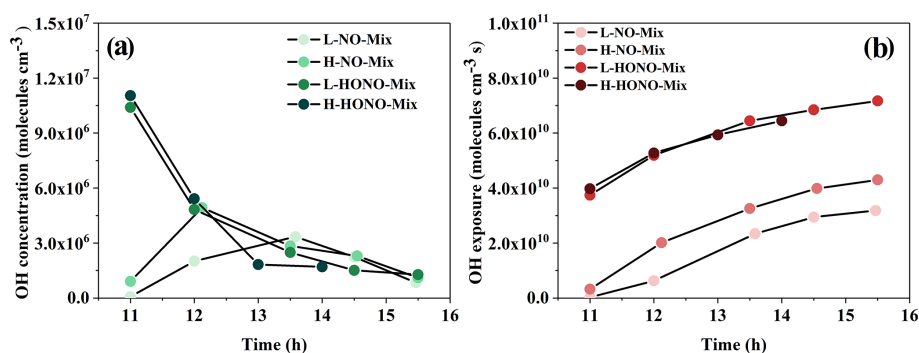
Figure 1. (a) OH radical concentration and **(b)** OH exposure versus time (hour) for mixture experiments. Each data point in this figure represents the average value (average OH concentration for **a**, average OH exposure for **b**) during the two sampling time periods. The point at 11:00 LST represents the average value of the data during the period from reaction initiation to 11:00 LST.

3.2 Ozone formation and gas phase products

3.2.1 Ozone formation

The ozone formation in the NO and HONO experiments is shown in Figs. S2 and S3. In order to conduct a specific analysis, the highest concentration of ozone generated by each reaction is selected and shown in Figs. 2 and S4. It can be clearly seen that the addition of SO$_2$ has little effect on ozone generation, and the ozone generation was analysed below from the perspective of the type of precursors, VOCs and NO$_x$, temperature, and the type of oxidant.

According to previous studies, the photochemical ozone formation potentials (OFPs) of VOCs are sensitive to their rate constants with OH radicals; i.e. VOCs with high reactivities have greater contributions to the ozone formation in the ambient atmosphere (Jenkin and Hayman, 1999). The reaction rate constants with OH at 298 K for 1,3,5-TMB and *n*-dodecane are 5.67×10^{-11} and 1.39×10^{-11} cm^3 molec.$^{-1}$ s^{-1}, respectively (Sivaramakrishnan and Michael, 2009; Atkinson and Arey, 2003). As shown in Fig. 2, compared with the mixture and 1,3,5-TMB reaction systems, the ozone concentration generated by the *n*-dodecane system is very low (< 8 ppb). For *n*-dodecane experiments, the formed ozone concentration under HONO conditions, the light pink area, is higher than that under NO conditions, the pink area. For 1,3,5-TMB experiments, the ozone concentration under HONO conditions in the light grey area is higher than that under NO conditions; the mixture experiments also show a similar phenomenon, the ozone concentration in the light purple area is higher than that in the purple area. This can also be explained by the OH exposure: as shown in Fig. 1, for similar NO$_x$ concentration, HONO conditions have higher OH radicals than NO experiments. Higher OH radicals would make the reaction system more oxidative, forming more RO$_2$ and HO$_2$ that can react with NO. This leads to competition in the reaction O$_3$ + NO → NO$_2$ + O$_2$ and causes the accumulation of ozone. It is also shown in Fig. 2 that the VOC-to-NO$_x$ ratio
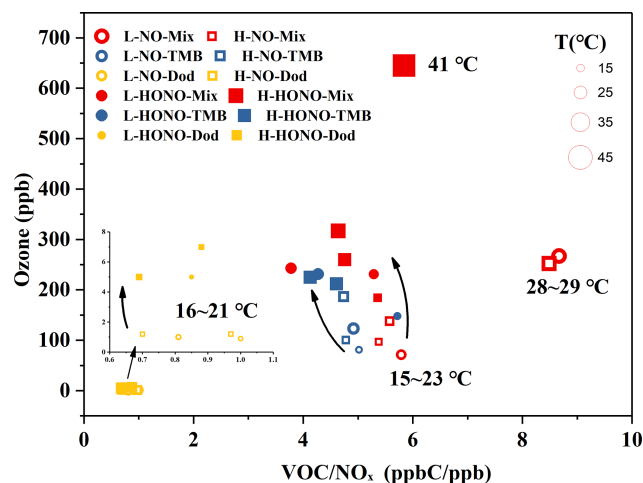
Figure 2. Ozone formation in the NO and HONO experiments. The temperature (T) and ozone concentration here refer to the maximum value during the reaction process. The yellow circles refer to NO-Dod experiments with low SO$_2$ concentration, and the yellow boxes refer to NO-Dod experiments with high SO$_2$ concentration. The yellow filled circles refer to HONO-Dod experiments with low SO$_2$ concentration, and the yellow filled boxes refer to HONO-Dod experiments with high SO$_2$ concentration. The blue circles refer to NO-TMB experiments with low SO$_2$ concentration, and the blue boxes refer to NO-TMB experiments with high SO$_2$ concentration. The blue filled circles refer to HONO-TMB experiments with low SO$_2$ concentration, and the blue filled boxes refer to HONO-TMB experiments with high SO$_2$ concentration. The red circles refer to NO-Mix experiments with low SO$_2$ concentration, and the red boxes refer to NO-Mix experiments with high SO$_2$ concentration. The red filled circles refer to HONO-Mix experiments with low SO$_2$ concentration, and the red filled boxes refer to HONO-Mix experiments with high SO$_2$ concentration.
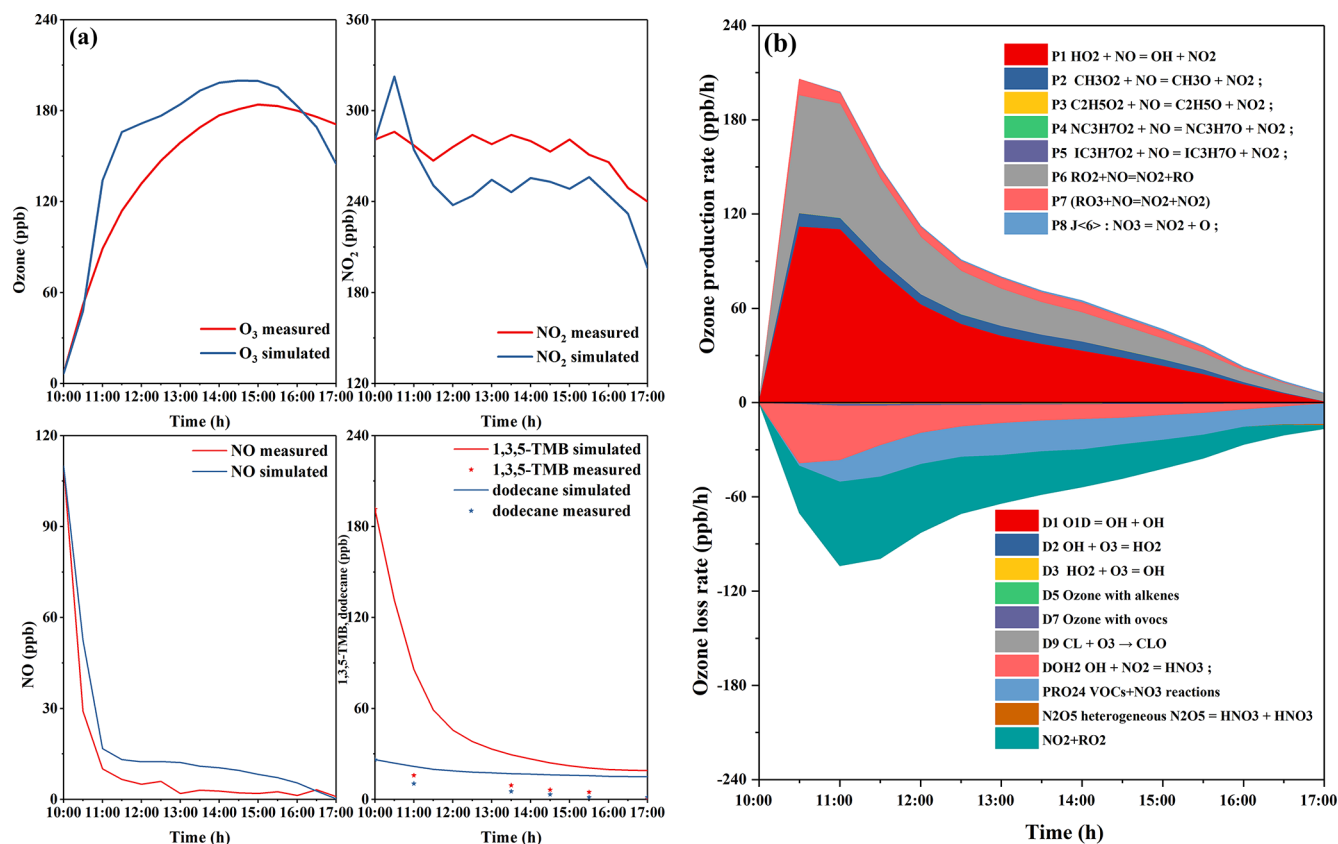
Figure 3. Concentration–time profiles of monitored and simulated **(a)** ozone, NO, NO$_2$, and 1,3,5-TMB and dodecane and **(b)** ozone formation and loss rates in the H-HONO-Mix-4 experiment.

(within the range of 1–10 ppbC ppb^{-1}) has little effect on the generation of ozone. However, temperature has a great influence on the formation of ozone. For experiment H-HONO-Mix-3, the temperature at noon was 41°, with a maximum ozone concentration of 645 ppb. In contrast, for the mixture experiments under similar VOC / NO$_x$ conditions but lower temperature (16–27°), the ozone concentration was 184–317 ppb. The reaction rates with OH increase with the rise of temperature (Atkinson and Arey, 2003), which in turn accelerate the oxidation processes. This may be a possible reason for the higher concentration of ozone generated under higher temperature conditions.

Figure 3 shows the concentration–time profiles of measured and simulated ozone and ozone formation and loss rates in H-HONO-Mix-4 experiment. The experiment was simulated with Master Chemical Mechanism MCM version 3.3 (http://mcm.leeds.ac.uk/MCM/, last access: 25 July 2022). The model was constrained with measured NO, NO$_2$, and HONO concentration. As shown in Fig. 3a, the ozone production is well represented by the model in the first 0.5 h; however the model starts to over-predict the O$_3$ concentration in the after 0.5 h. Metzger et al. (2008) also reported the phenomenon that the model over-predicted ozone at a later stage of the 1,3,5-TMB degradation

experiment, and the experiment was performed with an outdoor chamber. Meanwhile, the ozone photochemical budget cycle was simulated with the MCM model. The two major reactions of HO$_2$ + NO and RO$_2$ + NO control the photochemical generation of ozone; NO$_2$ + OH, NO$_2$ + RO$_2$, and VOCs + NO$_3$ reactions control the ozone consumption.

3.2.2 HONO concentration

For HONO experiments, HONO was introduced into the chamber with the same operation procedure, leading to similar HONO concentration. As shown in Fig. 4a, initial HONO concentrations exceed the device detection limit (70 ppb). When the enclosure was open, the HONO concentration decreased rapidly with the progress of the reaction in the first 2 h.

For NO experiments, the concentration of HONO first slowly increased at about 1 h after the photochemical reaction started and then decreased (Fig. 4b). At the same time, the particles began to increase significantly after 1 to 2 h after the start of the reaction, as revealed in Fig. S5. The increase in HONO concentration in NO experiments may have two reasons: the gas-phase reaction of NO with OH radicals and the heterogeneous reactions of NO$_2$ (Alicke, 2002; Wall
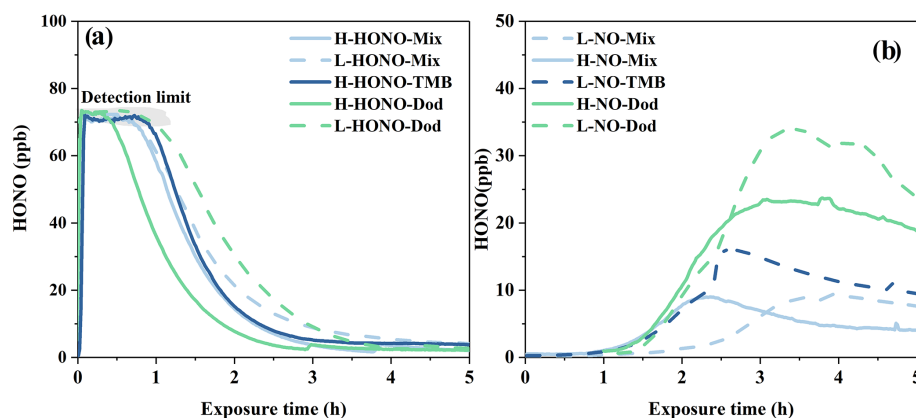
Figure 4. HONO concentration versus time during conducted experiments.
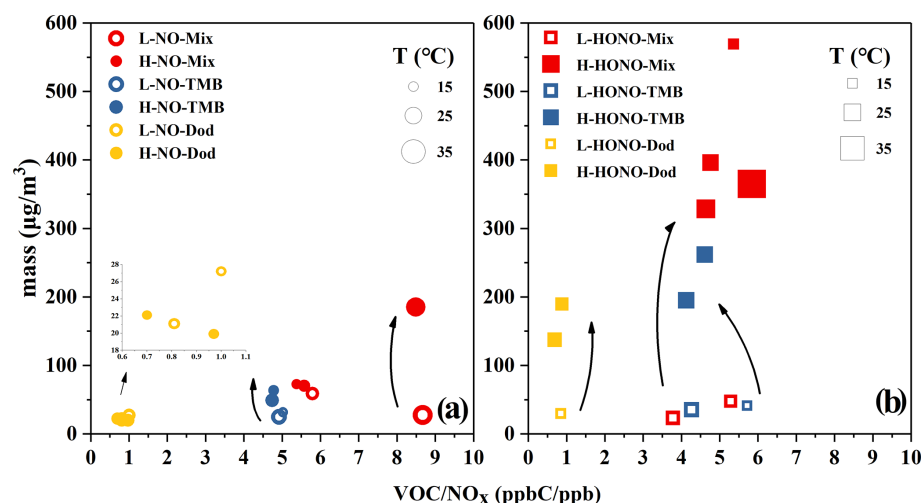

Figure 5. Particle formation of NO and HONO experiments. The temperature (T) and particle mass concentration here refer to the maximum value during the reaction process. The yellow circles refer to NO-Dod experiments with low SO$_2$ concentration, and the yellow filled circles refer to NO-Dod experiments with high SO$_2$ concentration. The blue circles refer to NO-TMB experiments with low SO$_2$ concentration, and the blue filled circles refer to NO-TMB experiments with high SO$_2$ concentration. The red circles refer to NO-Mix experiments with low SO$_2$ concentration, and the red filled circles refer to NO-Mix experiments with high SO$_2$ concentration.

and Harris, 2016). The concentrations of HONO generated in the NO-Mix and NO-1,3,5-TMB experiments are slightly lower than those in the NO-Dod experiments, and the NO-Mix experiments have the lowest HONO concentration. This is likely due to the difference in OH reactivity: the OH reactivity in the n-dodecane experiments (7.8–10.2 s^{-1}) is much lower than that in the 1,3,5-TMB (255–267.4 s^{-1}) and mixture experiments (255.9–278.6 s^{-1}), leading to weaker competition to OH + NO reaction.

3.3 Effect of NO$_x$ and SO$_2$ on particle formation

The particle formation (size distribution and max number concentration) in the NO and HONO experiments is shown in Figs. S5 and S6, and the corresponding max mass concentrations are shown in Figs. 5 and S7. When the max

number concentrations are above 10^5 # cm^{-3}, the banana-like-formation particles occur, especially in experiments with high SO$_2$ concentration. It is shown that the higher SO$_2$ concentration can promote particle production in both number (Figs. S5 and S6) and mass (Fig. 5) concentration. This finding is similar to previous studies with single precursors (Liu et al., 2016, 2019) and is likely due to the formation of sulfuric acid from SO$_2$ oxidation. First, sulfuric acid can participate in nucleation and enhance new particle formation (Sipila et al., 2010), resulting in higher particle number concentration. Second, sulfuric acid can promote acid-catalysed heterogeneous reactions and enhance the uptake of reactive organic compounds (Liu et al., 2016; Jang et al., 2002; Cao and Jang, 2007), which may lead to higher particle mass concentration. At last, the presence of SO$_2$ and sulfuric acid favour the formation of organo-sulfates (Liu et al., 2017,

2019; Chu et al., 2016), which is detected in our experiments (see Sect. 3.4).

In addition, it is found that the maximum values of particle number and mass concentration in the HONO reaction systems are higher than those of the NO reaction systems. In other words, under similar NO$_x$ and SO$_2$ concentrations, HONO conditions would be beneficial to the formation of particles. This phenomenon can be explained by higher OH exposure in HONO experiments, as shown in Fig. 1b. Higher OH exposure causes a higher consumption rate of the precursors and subsequent faster particle generation rates.

Figure 5 also shows the temperature effect on particle formation. For the same precursor, under similar VOC / NO$_x$ conditions, the lower the temperature, the higher the mass of particulate matter. Lower temperatures can affect the partitioning process of organic vapour and facilitate the formation of particles, which in turn increases the particle mass concentration in the reaction system, and this is consistent with previous experimental reports (Ding et al., 2017; Li et al., 2020; Sheehan and Bowman, 2001; Takekawa et al., 2003; Warren et al., 2009). Meanwhile, with the increase in the VOC/NO$_x$ ratio value, the particle mass concentration increases (S. Wang et al., 2020; K. Li et al., 2017).

The yellow boxes refer to HONO-Dod experiments with low SO$_2$ concentration, and the yellow filled boxes refer to HONO-Dod experiments with high SO$_2$ concentration. The blue boxes refer to HONO-TMB experiments with low SO$_2$ concentration, and the blue filled boxes refer to HONO-TMB experiments with high SO$_2$ concentration. The red boxes refer to HONO-Mix experiments with low SO$_2$ concentration, and the red filled boxes refer to HONO-Mix experiments with high SO$_2$ concentration.

3.4   Chemical compositions of particles

3.4.1   Inorganic chemical components

We analysed the inorganic components and organic components of the generated particles. Compared with the single-precursor systems, the particle mass concentration generated by the mixture system is the highest, so we selected the mixture system as the target and analysed the inorganic components. Overall, the amounts of sulfate and nitrate of HONO-Mix experiments are higher than those in NO-Mix experiments (HONO-Mix > NO-Mix). In the above reaction system, the generation pathway of nitric acid is mainly the reaction (Jarvis et al., 2009): $NO_2 + OH \rightarrow HNO_3$. With a similar NO$_x$ concentration, higher OH radicals are beneficial to the generation of nitric acid. As shown in Fig. 1, the HONO-Mix system has a higher concentration of OH radicals, which can explain the higher concentration of gas-phase nitric acid (Fig. 6b) and nitrate aerosol in this system (HONO-Mix$_{nitrate}$ > NO-Mix$_{nitrate}$). When SO$_2$ is added to the chamber, sulfate is formed by photooxidation of SO$_2$ in the reaction initiated by OH radical (Wang et al., 2021; Liu

et al., 2017) (HONO-Mix$_{sulfate}$ > NO-Mix$_{sulfate}$). For HONO experiments, the amounts of sulfate and nitrate of H-HONO-Mix are higher than those of L-HONO-Mix (H-HONO-Mix > L-HONO-Mix), especially for sulfate. As mentioned above, higher OH concentration is beneficial to nitrate formation, and higher SO$_2$ will promote the formation of sulfate in the system. For NO experiments, the amounts of sulfate and nitrate of H-NO-Mix are also higher than those of L-NO-Mix (H-NO-Mix > L-NO-Mix), with the L-NO-Mix experiment forming negligible sulfate and nitrate. As shown in Fig. 1, L-NO-Mix has the lowest OH exposure, and the SO$_2$ concentration is also low, which can explain its low nitrate and sulfate concentration.

As shown in Fig. 6a, compared with the total mass concentration of the resulting particles, the sulfate and nitrate production amounts under the four conditions are very low, so we focus on analysing the organic components in the particles, including the analysis of functional groups by infrared spectroscopy and the analysis of chemical components by mass spectrometry.

3.4.2   Organic chemical composition

In order to analyse the functional groups of the particles, we dissolved the collected particles with methanol and detected them with an infrared spectrometer. Figure S8 and Table S3 show the IR spectra of aerosols formed under NO conditions and HONO conditions. According to the positions of the absorption peak in the IR spectra, different functional groups were assigned. The bold peak at 3360 cm^{-1} is assigned to the characteristic peak of C–OH in alcohol, the broadband at 3100–3300 cm^{-1} (3192 cm^{-1}) originates from the O–H stretching vibration of hydroxyl and carboxyl groups (Liu et al., 2017; Coury and Dillner, 2008), and the absorption around 3000–3200 cm^{-1} in the 1,3,5-TMB and Mixture experiments can represent the stretching vibration of C–H bonds in aromatics (Holes et al., 1997). The peaks around 1633-1660 cm^{-1} are assigned to the C = O stretching vibrations of ketones, aldehydes, and carboxylic acids (Coury and Dillner, 2008). The peaks at 2960 cm^{-1} correspond to CH$_3$ stretching vibration in alkanes, 2921 and 2850 cm^{-1} correspond to CH$_2$ stretching vibration in alkanes (Holes et al., 1997), and the broadbands around 1415–1465 cm^{-1} represent the deformation vibrations of methylene and methyl groups. The peak at 1268 cm^{-1} is assigned to the $-ONO_2$ stretching in nitrate ester (Holes et al., 1997; Jia and Xu, 2014; Li et al., 2021b). According to literature reports, peaks in the range of 1000–1200 cm^{-1} are assigned to the absorption peak of sulfate (Wu et al., 2013), peaks around 1040–1070 cm^{-1} represent the absorption band of S = O in organic compounds (Chihara, 1958), and the peak at 1100 cm^{-1} corresponds to the sulfate group in sulfate and organic compounds (Liu et al., 2017). The above analysis confirmed the presence of carboxylic acids, alcohols, nitrates,
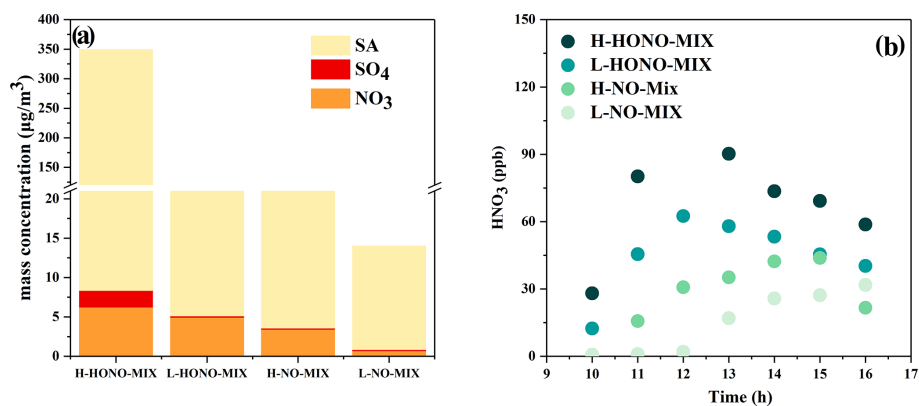
Figure 6. (a) The measured mass concentration of sulfate, nitrate, and total secondary aerosol in the particle phase. The data used in this plot are the average of the hour in which the mass concentration was the greatest. SA is the abbreviation of secondary aerosol. **(b)** The concentration of gas-phase nitric acid in the mixture system.
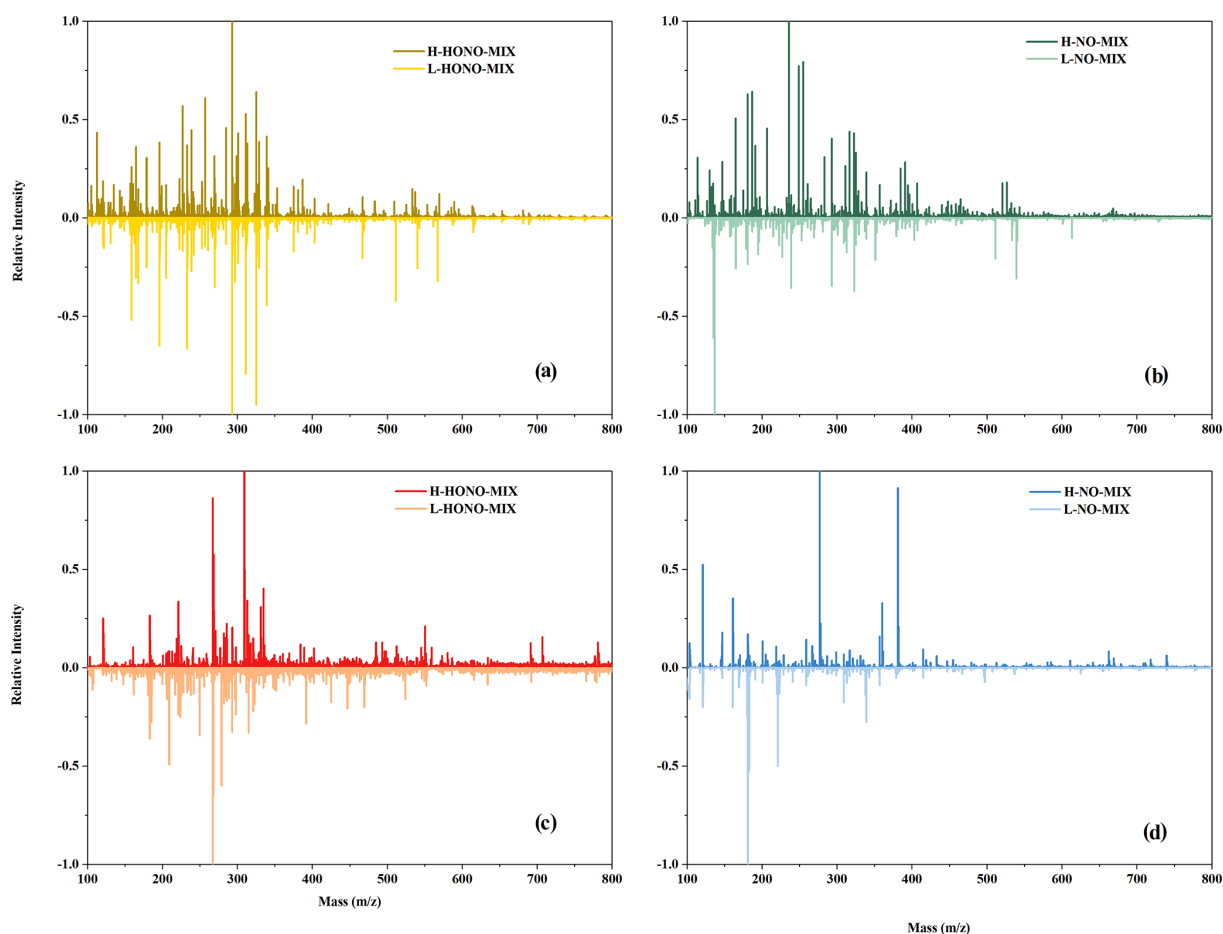
Figure 7. Mass spectra of mixture experiments: **(a)** HONO mixture experiments in negative mode, **(b)** NO mixture experiments in negative mode, **(c)** HONO mixture experiments in positive mode, and **(d)** NO mixture experiments in positive mode. The y axis is the relative intensity normalised by dividing by the maximum signal strength of the mass spectra.

sulfates, aldehydes, and ketones in aerosols derived from both the NO and HONO conditions with high or low SO$_2$.

In order to conduct a more in-depth analysis of the organic compounds in the particles, we performed mass spectrometry analysis (Fig. 7). In a previous study (Li et al., 2021b), we have shown that the chemical interactions between intermediate products from n-dodecane and 1,3,5-TMB can promote particle formation in the mixture experiments under HONO conditions. In this study, we focus on the influence of SO$_2$ and the concentration of OH radicals on the formation of particles, and we analysed the formed particles of mixture experiments.

The products of mixture experiments were detected by ESI-Q-ToF-MS in both negative (Fig. 7a and b) and positive (Fig. 7c and d) modes. Compared to NO-Mix, more products with larger-molecular-weights are formed under HONO-Mix. This is probably due to the higher OH concentration in the HONO experiments (Fig. 1), which favours the formation of large molecular weight products through functionalisation reactions. Lambe et al. (2012) reported that when the OH radical exposure was within $(5–6) \times 10^{11}$ molec. cm^{-3} s, the SOA yield of alkanes precursors (C$_{10}$ and C$_{15}$) exhibited an increase as a function of OH radical exposure, and the increase correlated with an increase in oxygen content.

Meanwhile, organo-sulfates and organo-nitrates are formed in the mixture experiments, as shown in Table S4. It is found that larger concentrations of organo-nitrates are formed under HONO conditions compared with NO conditions. The primary formation pathway of organo-nitrates is the reaction of RO$_2$ + NO, and the RO$_2$ is mainly formed through the reaction of organic gases with OH radicals (Li et al., 2022; Tsiligiannis et al., 2019). Under HONO conditions, a higher concentration of OH radical is formed (Fig. 1), so more RO$_2$ will exist in HONO experiments, and thus more organo-nitrates will be formed. In addition, high-SO$_2$ conditions are more conducive to the formation of organo-sulfates, e.g. H-NO-Mix$_{organo-sulfate}$ > L-NO-Mix$_{organo-sulfate}$ (Table S4). As discussed in Sect. 3.4.1, sulfate is formed by reaction of the SO$_2$ + OH radical (Wang et al., 2021; Liu et al., 2017), and higher SO$_2$ would facilitate the formation of sulfate in the experiments. According to previous studies (Yang et al., 2020), organo-sulfates are mainly formed through the reaction of sulfate with compounds containing OH bonds or ether bonds. Therefore, higher SO$_2$ would facilitate the formation of organo-sulfates.

The proposed reaction mechanism of mixture experiment in the presence of NO$_x$ and SO$_2$ is shown in Fig. 8. The products derived from n-dodecane are oxygen-containing organic compounds (aldehydes, ketones, alcohols, carboxylic acid, etc.), organic nitrates, and organo-sulfates; the products derived from 1,3,5-TMB are also multifunctional products containing carbonyl, acid, alcohol, nitrate, and sulfate functional groups. For the mixture experiment, the intermediate multifunctional products can react with each other, and high-molecular-weight oligomers are thus produced. As an exam-

ple, C$_{14}$H$_{21}$NO$_5$ might be the product from the reaction of a phenol from 1,3,5-TMB (C$_9$H$_{12}$O) and an aldehyde from n-dodecane (C$_5$H$_{10}$O).

4 Conclusion and implications

In the present work, a large-scale outdoor smog chamber was applied to study the effect of inorganic gases (SO$_2$ and NO$_x$) on the photochemical process of mixed anthropogenic organic gases, i.e. n-dodecane and 1,3,5-trimethylbeneze. The OH concentration under HONO conditions is higher than that under classic NO$_x$ conditions at similar measured NO$_x$ concentrations. The ozone formation is affected by the reaction precursors, the concentration of OH radicals, and the temperature: precursors with higher ozone formation potential also contribute significantly to ozone formation in the mixture reaction system; higher temperature and higher OH concentration are beneficial to the formation of ozone in the reactions. In contrast, the presence of SO$_2$ has little effect on ozone formation.

However, the presence of SO$_2$ can greatly promote the formation of particles in both number and mass concentration, likely due to the enhanced new particle formation and acid-catalysed heterogeneous reactions from the formation of sulfuric acid and the formation of organo-sulfates (Liu et al., 2017, 2019; K. Li et al., 2017). In addition, higher OH radical concentration and lower temperature are also beneficial to the formation of particles. For the particle composition, the content of inorganic nitrate and sulfate under the HONO conditions was higher than that under the NO conditions, although organic aerosols dominate the total secondary aerosols. The organo-sulfates and organo-nitrates are detected in the formed particles, and the presence of SO$_2$ is found to promote the formation of organo-sulfates.

Based on the molecular composition detected in the mixed experiments, we propose a mechanism of high-molecular-weight compound formation from the reaction of intermediate products originating from different precursors. This indicates that high-molecular-weight compounds (some of them are N- and/or S-containing species) in the ambient environment might be formed from the interactions of different precursors in the presence of NO$_x$ and SO$_2$. When analysing the source of the detected aerosol species in the atmospheric environment, possible interactions from different VOC types need to be considered. In addition, the interactions between VOCs should be taken into account when evaluating the particle formation potential based on the monitored VOCs and oxidants.

This study provides the first attempt to investigate the role of SO$_2$ in the oxidation of mixed anthropogenic organic gases with various OH concentrations and temperature conditions. The results here can improve our understanding in the chemical processes that lead to ozone and secondary particle formation in the complex urban areas influenced by
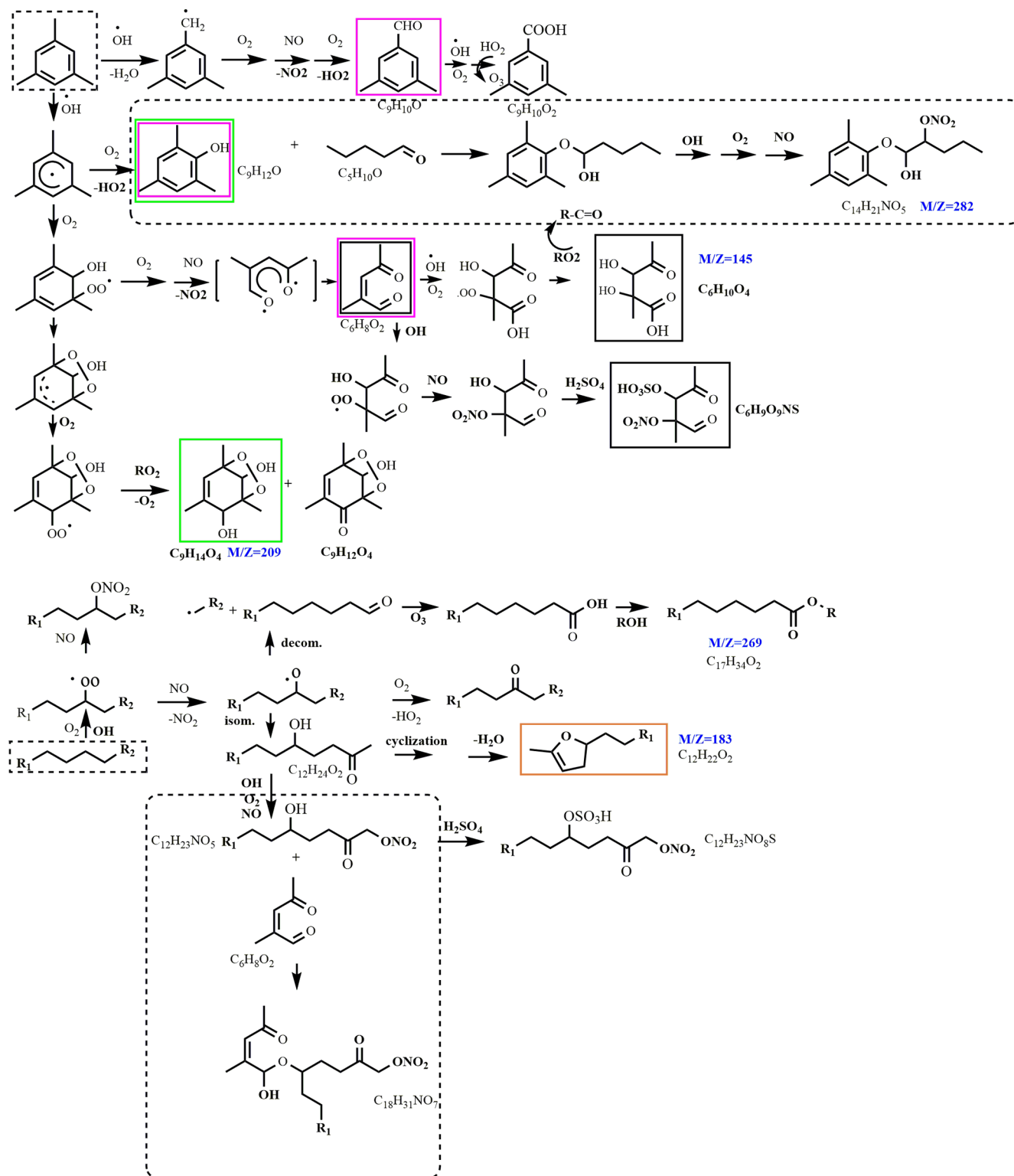
Figure 8. Proposed reaction mechanism of the mixture experiment in the presence of NO_x and SO_2 (R_1 and R_2 are alkyl groups). Compounds in blue are detected by ESI-Q-ToF-MS in this work; solid boxed compounds are detected by previous studies (black, Yang et al., 2020; purple, M. Huang et al., 2014; green, Sato et al., 2019; orange, Yee et al., 2013). The reactions in the dotted boxes are the proposed reaction paths of the mixture experiment.

complex emissions (including vehicle exhaust, coal combustion, etc.). More in-depth and detailed research on the mixture reaction systems with atmospheric-relevant conditions should be carried out in the future to deepen our understanding of the physical and chemical processes in the oxidation of organic vapours in the real atmosphere.

Author contributions. JLL, HL, and MFG designed the experiments. JLL conducted the experiments with help from HZ, XZ, YYJ, WHC, and YXK. JLL analysed the data and wrote the paper, with contributions from KL, HL, and MFG, and YXC, YQR, YJZ, HJZ, RG, ZHW, FB, XC, XZW, and WGW commented on the paper.

References

Alicke, B.: Impact of nitrous acid photolysis on the total hydroxyl radical budget during the Limitation of Oxidant Production/Pianura Padana Produzione di Ozono study in Milan, J. Geophys. Res., 107, 8196, https://doi.org/10.1029/2000jd000075, 2002.

Atkinson, R. and Arey, J.: Atmospheric degradation of volatile organic compounds, Chem. Rev., 103, 4605–4638, https://doi.org/10.1021/cr0206420, 2003.

Barmet, P., Dommen, J., DeCarlo, P. F., Tritscher, T., Praplan, A. P., Platt, S. M., Prévôt, A. S. H., Donahue, N. M., and Baltensperger, U.: OH clock determination by proton transfer reaction mass spectrometry at an environmental chamber, Atmos. Meas. Tech., 5, 647–656, https://doi.org/10.5194/amt-5-647-2012, 2012.

Cai, S., Zhu, L., Wang, S., Wisthaler, A., Li, Q., Jiang, J., and Hao, J.: Time-resolved intermediate-volatility and semivolatile organic compound emissions from household coal combustion in Northern China, Environ. Sci. Technol., 53, 9269–9278, https://doi.org/10.1021/acs.est.9b00734, 2019.

Cao, G. and Jang, M.: Effects of particle acidity and UV light on secondary organic aerosol formation from oxidation of aromatics in the absence of NO$_x$, Atmos. Environ., 41, 7603–7613, https://doi.org/10.1016/j.atmosenv.2007.05.034, 2007.

Chen, T., Liu, Y., Ma, Q., Chu, B., Zhang, P., Liu, C., Liu, J., and He, H.: Significant source of secondary aerosol: formation from gasoline evaporative emissions in the presence of SO$_2$ and NH$_3$, Atmos. Chem. Phys., 19, 8063–8081, https://doi.org/10.5194/acp-19-8063-2019, 2019.

Chen, T., Xue, L., Zheng, P., Zhang, Y., Liu, Y., Sun, J., Han, G., Li, H., Zhang, X., Li, Y., Li, H., Dong, C., Xu, F., Zhang, Q., and Wang, W.: Volatile organic compounds and ozone air pollution in an oil production region in northern China, Atmos. Chem. Phys., 20, 7069–7086, https://doi.org/10.5194/acp-20-7069-2020, 2020.

Chen, Y., Wang, W., Lian, C., Peng, C., Zhang, W., Li, J., Liu, M., Shi, B., Wang, X., and Ge, M.: Evaluation and impact factors of indoor and outdoor gas-phase nitrous acid under different environmental conditions, J. Environ. Sci., 95, 165–171, https://doi.org/10.1016/j.jes.2020.03.048, 2020.

Cheng, J., Su, J., Cui, T., Li, X., Dong, X., Sun, F., Yang, Y., Tong, D., Zheng, Y., Li, Y., Li, J., Zhang, Q., and He, K.: Dominant role of emission reduction in PM$_{2.5}$ air quality improvement in Beijing during 2013–2017: a model-based decomposition analysis, Atmos. Chem. Phys., 19, 6125–6146, https://doi.org/10.5194/acp-19-6125-2019, 2019.

Chihara, G.: Characteristic infrared absorption band of organic sulfate esters, Chem. Pharm. Bull., 6, 114, https://doi.org/10.1248/cpb.6.114, 1958.

Chu, B., Zhang, X., Liu, Y., He, H., Sun, Y., Jiang, J., Li, J., and Hao, J.: Synergetic formation of secondary inorganic and organic aerosol: effect of SO$_2$ and NH$_3$ on particle formation and growth, Atmos. Chem. Phys., 16, 14219–14230, https://doi.org/10.5194/acp-16-14219-2016, 2016.

Coury, C. and Dillner, A. M.: A method to quantify organic functional groups and inorganic compounds in ambient aerosols using attenuated total reflectance FTIR spectroscopy and multivariate chemometric techniques, Atmos. Environ., 42, 5923–5932, https://doi.org/10.1016/j.atmosenv.2008.03.026, 2008.

Crouse, D. L., Peters, P. A., van Donkelaar, A., Goldberg, M. S., Villeneuve, P. J., Brion, O., Khan, S., Atari, D. O., Jerrett, M., Pope, C. A., Brauer, M., Brook, J. R., Martin, R. V., Stieb, D., and Burnett, R. T.: Risk of nonaccidental and cardiovascular mortality in relation to long-term exposure to low concentrations of fine particulate matter: a Canadian national-level cohort study, Environ. Health Perspect., 120, 708–714, https://doi.org/10.1289/ehp.1104049, 2012.

Deng, W., Hu, Q., Liu, T., Wang, X., Zhang, Y., Song, W., Sun, Y., Bi, X., Yu, J., Yang, W., Huang, X., Zhang, Z., Huang, Z., He, Q., Mellouki, A., and George, C.: Primary particulate emissions and secondary organic aerosol (SOA) formation from idling diesel vehicle exhaust in China, Sci. Total Environ., 593–594, 462–469, https://doi.org/10.1016/j.scitotenv.2017.03.088, 2017.

Ding, X., Zhang, Y. Q., He, Q. F., Yu, Q. Q., Wang, J. Q., Shen, R. Q., Song, W., Wang, Y. S., and Wang, X. M.: Significant Increase of Aromatics-Derived Secondary Organic Aerosol during Fall to Winter in China, Environ. Sci. Technol., 51, 7432–7441, https://doi.org/10.1021/acs.est.6b06408, 2017.

Docherty, K. S., Yaga, R., Preston, W., Jaoui, M., Reidel, T. P., Offenberg, J. H., Kleindienst, T. E., and Lewandowski, M.: Relative contributions of selected multigeneration products to chamber SOA formed from photooxidation of a range (C_{10}–C_{17}) of n-alkanes under high NO$_x$ conditions, Atmos. Environ., 244, 117976, https://doi.org/10.1016/j.atmosenv.2020.117976, 2021.

Fahnestock, K. A. S., Yee, L. D., Loza, C. L., Coggon, M. M., Schwantes, R., Zhang, X., Dalleska, N. F., and Seinfeld, J. H.: Secondary organic aerosol composition from C-12 alkanes, J. Phys. Chem. A, 119, 4281–4297, https://doi.org/10.1021/jp501779w, 2015.

Fang, H., Huang, X., Zhang, Y., Pei, C., Huang, Z., Wang, Y., Chen, Y., Yan, J., Zeng, J., Xiao, S., Luo, S., Li, S., Wang, J., Zhu, M., Fu, X., Wu, Z., Zhang, R., Song, W., Zhang, G., Hu, W., Tang, M., Ding, X., Bi, X., and Wang, X.: Measurement report: Emissions of intermediate-volatility organic compounds from vehicles under real-world driving conditions in an urban tunnel, Atmos. Chem. Phys., 21, 10005–10013, https://doi.org/10.5194/acp-21-10005-2021, 2021.

Gao, M., Liu, Z., Zheng, B., Ji, D., Sherman, P., Song, S., Xin, J., Liu, C., Wang, Y., Zhang, Q., Xing, J., Jiang, J., Wang, Z., Carmichael, G. R., and McElroy, M. B.: China's emission control strategies have suppressed unfavorable influences of climate on wintertime PM$_{2.5}$ concentrations in Beijing since 2002, Atmos. Chem. Phys., 20, 1497–1505, https://doi.org/10.5194/acp-20-1497-2020, 2020.

Gentner, D. R., Isaacman, G., Worton, D. R., Chan, A. W. H., Dallmann, T. R., Davis, L., Liu, S., Day, D. A., Russell, L. M., Wilson, K. R., Weber, R., Guha, A., Harley, R. A., and Goldstein, A. H.: Elucidating secondary organic aerosol from diesel and gasoline vehicles through detailed characterization of organic carbon emissions, P. Natl. Acad. Sci. USA, 109, 18318–18323, https://doi.org/10.1073/pnas.1212272109, 2012.

Guo, S., Hu, M., Wang, Z. B., Slanina, J., and Zhao, Y. L.: Size-resolved aerosol water-soluble ionic compositions in the summer of Beijing: implication of regional secondary formation, Atmos. Chem. Phys., 10, 947–959, https://doi.org/10.5194/acp-10-947-2010, 2010.

Holes, A., Eusebi, A., Grosjean, D., and Allen, D. T.: FTIR analysis of aerosol formed in the photooxidation of 1,3,5-trimethylbenzene, Aerosol Sci. Tech., 26, 516–526, https://doi.org/10.1080/02786829708965450, 1997.

Hu, W., Zhou, H., Chen, W., Ye, Y., Pan, T., Wang, Y., Song, W., Zhang, H., Deng, W., Zhu, M., Wang, C., Wu, C., Ye, C., Wang, Z., Yuan, B., Huang, S., Shao, M., Peng, Z., Day, D. A., Campuzano-Jost, P., Lambe, A. T., Worsnop, D. R., Jimenez, J. L., and Wang, X.: Oxidation flow reactor results in a Chinese megacity emphasize the important contribution of S/IVOCs to ambient SOA formation, Environ. Sci. Technol., 56, 6880–6893, https://doi.org/10.1021/acs.est.1c03155, 2021.

Huang, M., Hu, C., Guo, X., Gu, X., Zhao, W., Wang, Z., Fang, L., and Zhang, W.: Chemical composition of gas and particle–phase products of OH-initiated oxidation of 1,3,5-trimethylbenzene, Atmos. Pollut. Res., 5, 73–78, https://doi.org/10.5094/apr.2014.009, 2014.

Huang, R. J., Zhang, Y., Bozzetti, C., Ho, K. F., Cao, J. J., Han, Y., Daellenbach, K. R., Slowik, J. G., Platt, S. M., Canonaco, F., Zotter, P., Wolf, R., Pieber, S. M., Bruns, E. A., Crippa, M., Ciarelli, G., Piazzalunga, A., Schwikowski, M., Abbaszade, G., Schnelle-Kreis, J., Zimmermann, R., An, Z., Szidat, S., Baltensperger, U., El Haddad, I., and Prevot, A. S.: High secondary aerosol contribution to particulate pollution during haze events in China, Nature, 514, 218–222, https://doi.org/10.1038/nature13774, 2014.

Jang, M. S., Czoschke, N. M., Lee, S., and Kamens, R. M.: Heterogeneous atmospheric aerosol production by acid-catalyzed particle-phase reactions, Science, 298, 814–817, https://doi.org/10.1126/science.1075798, 2002.

Jaoui, M., Edney, E. O., Kleindienst, T. E., Lewandowski, M., Offenberg, J. H., Surratt, J. D., and Seinfeld, J. H.: Formation of secondary organic aerosol from irradiated alpha-pinene/toluene/NO$_x$ mixtures and the effect of isoprene and sulfur dioxide, J. Geophys. Res.-Atmos., 113, D09303, https://doi.org/10.1029/2007jd009426, 2008.

Jarvis, J. C., Hastings, M. G., Steig, E. J., and Kunasek, S. A.: Isotopic ratios in gas-phase HNO$_3$ and snow nitrate at Summit, Greenland, J. Geophys. Res., 114, D17301, https://doi.org/10.1029/2009jd012134, 2009.

Jenkin, M. E. and Hayman, G., D.: Photochemical ozone creation potentials for oxygenated volatile organic compounds: sensitivity to variations in kinetic and mechanistic parameter, Atmos. Environ., 33, 1275–1293, 1999.

Jia, L. and Xu, Y.: Effects of Relative Humidity on ozone and secondary organic aerosol formation from the photooxidation of benzene and ethylbenzene, Aerosol Sci. Tech., 48, 1–12, https://doi.org/10.1080/02786826.2013.847269, 2014.

Jimenez, J. L., Canagaratna, M. R., Donahue, N. M., Prevot, A. S., Zhang, Q., Kroll, J. H., DeCarlo, P. F., Allan, J. D., Coe, H., Ng, N. L., Aiken, A. C., Docherty, K. S., Ulbrich, I. M., Grieshop, A. P., Robinson, A. L., Duplissy, J., Smith, J. D., Wilson, K. R., Lanz, V. A., Hueglin, C., Sun, Y. L., Tian, J., Laaksonen, A., Raatikainen, T., Rautiainen, J., Vaattovaara, P., Ehn, M., Kulmala, M., Tomlinson, J. M., Collins, D. R., Cubison, M. J., Dunlea, E. J., Huffman, J. A., Onasch, T. B., Alfarra, M. R., Williams, P. I., Bower, K., Kondo, Y., Schneider, J., Drewnick, F., Borrmann, S., Weimer, S., Demerjian, K., Salcedo, D., Cottrell, L., Griffin, R., Takami, A., Miyoshi, T., Hatakeyama, S., Shimono, A., Sun, J. Y., Zhang, Y. M., Dzepina, K., Kimmel, J. R., Sueper, D., Jayne, J. T., Herndon, S. C., Trimborn, A. M., Williams, L. R., Wood, E. C., Middlebrook, A. M.,

Kolb, C. E., Baltensperger, U., and Worsnop, D. R.: Evolution of organic aerosols in the atmosphere, Science, 326, 1525–1529, https://doi.org/10.1126/science.1180353, 2009.

Kanakidou, M., Seinfeld, J. H., Pandis, S. N., Barnes, I., Dentener, F. J., Facchini, M. C., Van Dingenen, R., Ervens, B., Nenes, A., Nielsen, C. J., Swietlicki, E., Putaud, J. P., Balkanski, Y., Fuzzi, S., Horth, J., Moortgat, G. K., Winterhalter, R., Myhre, C. E. L., Tsigaridis, K., Vignati, E., Stephanou, E. G., and Wilson, J.: Organic aerosol and global climate modelling: a review, Atmos. Chem. Phys., 5, 1053–1123, https://doi.org/10.5194/acp-5-1053-2005, 2005.

Kleindienst, Tadeusz E., Edney, E. O., LewandowskiI, M., Offenberg, J. H., and Jaoui, M.: Secondary organic carbon and aerosol yields from the irradiations of isoprene and α-pinene in the presence of NO$_x$ and SO$_2$, Environ. Sci. Technol., 40, 3807–3812, 2006.

Lambe, A. T., Onasch, T. B., Croasdale, D. R., Wright, J. P., Martin, A. T., Franklin, J. P., Massoli, P., Kroll, J. H., Canagaratna, M. R., Brune, W. H., Worsnop, D. R., and Davidovits, P.: Transitions from functionalization to fragmentation reactions of laboratory secondary organic aerosol (SOA) generated from the OH oxidation of alkane precursors, Environ. Sci. Technol., 46, 5430–5437, https://doi.org/10.1021/es300274t, 2012.

Lamkaddam, H., Gratien, A., Ropion, M., Pangui, E., and Doussin, J. F.: Kinetic study of the temperature dependence of OH-initiated oxidation of n-dodecane, J. Phys. Chem. A, 123, 9462–9468, https://doi.org/10.1021/acs.jpca.9b07704, 2019.

Lamkaddam, H., Gratien, A., Pangui, E., David, M., Peinado, F., Polienor, J.-M., Jerome, M., Cazaunau, M., Gaimoz, C., Picquet-Varrault, B., Kourtchev, I., Kalberer, M., and Doussin, J.-F.: Role of relative humidity in the secondary organic aerosol formation from high-NO$_x$ photooxidation of long-chain alkanes: n-Dodecane case study, ACS Earth Space Chem., 4, 2414–2425, https://doi.org/10.1021/acsearthspacechem.0c00265, 2020.

Li, H., Zhang, Q., Zhang, Q., Chen, C., Wang, L., Wei, Z., Zhou, S., Parworth, C., Zheng, B., Canonaco, F., Prévôt, A. S. H., Chen, P., Zhang, H., Wallington, T. J., and He, K.: Wintertime aerosol chemistry and haze evolution in an extremely polluted city of the North China Plain: significant contribution from coal and biomass combustion, Atmos. Chem. Phys., 17, 4751–4768, https://doi.org/10.5194/acp-17-4751-2017, 2017.

Li, J.: MCM datasets, figshare [data set], https://doi.org/10.6084/m9.figshare.20501796.v1, 2022a.

Li, J.: Effects of OH radical and SO$_2$ concentrations on photochemical reactions of mixed anthropogenic organic gases, figshare [data set], https://doi.org/10.6084/m9.figshare.20437134.v4, 2022b.

Li, J., Li, K., Wang, W., Wang, J., Peng, C., and Ge, M.: Optical properties of secondary organic aerosols derived from long-chain alkanes under various NO$_x$ and seed conditions, Sci. Total Environ., 579, 1699–1705, https://doi.org/10.1016/j.scitotenv.2016.11.189, 2017.

Li, J., Wang, W., Li, K., Zhang, W., Peng, C., Zhou, L., Shi, B., Chen, Y., Liu, M., Li, H., and Ge, M.: Temperature effects on optical properties and chemical composition of secondary organic aerosol derived from n-dodecane, Atmos. Chem. Phys. 20, 8123–8137, https://doi.org/10.5194/acp-20-8123-2020, 2020.

Li, J., Wang, W., Li, K., Zhang, W., Peng, C., Liu, M., Chen, Y., Zhou, L., Li, H., and Ge, M.: Effect of chemical struc-

ture on optical properties of secondary organic aerosols derived from C$_{12}$ alkanes, Sci. Total Environ., 751, 141620, https://doi.org/10.1016/j.scitotenv.2020.141620, 2021a.

Li, J., Li, H., Li, K., Chen, Y., Zhang, H., Zhang, X., Wu, Z., Liu, Y., Wang, X., Wang, W., and Ge, M.: Enhanced secondary organic aerosol formation from the photo-oxidation of mixed anthropogenic volatile organic compounds, Atmos. Chem. Phys., 21, 7773–7789, https://doi.org/10.5194/acp-21-7773-2021, 2021b.

Li, J., Li, H., Wang, X., Wang, W., Ge, M., Zhang, H., Zhang, X., Li, K., Chen, Y., Wu, Z., Chai, F., Meng, F., Mu, Y., Mellouki, A., Bi, F., Zhang, Y., Wu, L., and Liu, Y.: A Large-Scale Outdoor Atmospheric Simulation Smog Chamber for Studying Atmospheric Photochemical Processes: Characterization and Preliminary Application, J. Environ. Sci., 102, 185–197, 2021c.

Li, J., Li, K., Li, H., Wang, X., Wang, W., Wang, K., and Ge, M.: Long-chain alkanes in the atmosphere: A review, J. Environ. Sci., 114, 37–52, https://doi.org/10.1016/j.jes.2021.07.021, 2022.

Li, K., Liggio, J., Lee, P., Han, C., Liu, Q., and Li, S.-M.: Secondary organic aerosol formation from α-pinene, alkanes, and oil-sands-related precursors in a new oxidation flow reactor, Atmos. Chem. Phys., 19, 9715–9731, https://doi.org/10.5194/acp-19-9715-2019, 2019a.

Li, K., Liggio, J., Han, C., Liu, Q., Moussa, S. G., Lee, P., and Li, S. M.: Understanding the Impact of High-NO$_x$ Conditions on the Formation of Secondary Organic Aerosol in the Photooxidation of Oil Sand-Related Precursors, Environ. Sci. Technol., 53, 14420–14429, https://doi.org/10.1021/acs.est.9b05404, 2019b.

Li, K., Chen, L., White, S. J., Han, K., Lv, B., Bao, K., Wu, X., Gao, X., Azzi, M., and Cen, K.: Effect of nitrogen oxides (NO and NO$_2$) and toluene on SO$_2$ photooxidation, nucleation and growth: A smog chamber study, Atmos. Res., 192, 38–47, https://doi.org/10.1016/j.atmosres.2017.03.017, 2017c.

Li, K., Wentzell, J. J. B., Liu, Q., Leithead, A., Moussa, S. G., Wheeler, M. J., Han, C., Lee, P., Li, S.-M., and Liggio, J.: Evolution of atmospheric total organic carbon from petrochemical mixtures, Environ. Sci. Technol., 55, 12841–12851, https://doi.org/10.1021/acs.est.1c02620, 2021.

Liggio, J. and Li, S. M.: A new source of oxygenated organic aerosol and oligomers, Atmos. Chem. Phys., 13, 2989–3002, https://doi.org/10.5194/acp-13-2989-2013, 2013.

Liu, C., Chen, T., Liu, Y., Liu, J., He, H., and Zhang, P.: Enhancement of secondary organic aerosol formation and its oxidation state by SO$_2$ during photooxidation of 2-methoxyphenol, Atmos. Chem. Phys., 19, 2687–2700, https://doi.org/10.5194/acp-19-2687-2019, 2019.

Liu, S., Jia, L., Xu, Y., Tsona, N. T., Ge, S., and Du, L.: Photooxidation of cyclohexene in the presence of SO$_2$: SOA yield and chemical composition, Atmos. Chem. Phys., 17, 13329–13343, https://doi.org/10.5194/acp-17-13329-2017, 2017.

Liu, T., Wang, X., Hu, Q., Deng, W., Zhang, Y., Ding, X., Fu, X., Bernard, F., Zhang, Z., Lü, S., He, Q., Bi, X., Chen, J., Sun, Y., Yu, J., Peng, P., Sheng, G., and Fu, J.: Formation of secondary aerosols from gasoline vehicle exhaust when mixing with SO$_2$, Atmos. Chem. Phys., 16, 675–689, https://doi.org/10.5194/acp-16-675-2016, 2016.

Loza, C. L., Craven, J. S., Yee, L. D., Coggon, M. M., Schwantes, R. H., Shiraiwa, M., Zhang, X., Schilling, K. A., Ng, N. L., Canagaratna, M. R., Ziemann, P. J., Flagan, R. C., and Seinfeld, J. H.: Secondary organic aerosol yields of 12-carbon alkanes, At-

mos. Chem. Phys., 14, 1423–1439, https://doi.org/10.5194/acp-14-1423-2014, 2014.

Mao, J., Ren, X., Brune, W. H., Olson, J. R., Crawford, J. H., Fried, A., Huey, L. G., Cohen, R. C., Heikes, B., Singh, H. B., Blake, D. R., Sachse, G. W., Diskin, G. S., Hall, S. R., and Shetter, R. E.: Airborne measurement of OH reactivity during INTEX-B, Atmos. Chem. Phys., 9, 163–173, https://doi.org/10.5194/acp-9-163-2009, 2009.

MCM – The Master Chemical Mechanism: Welcome to the MCM website, http://mcm.york.ac.uk/, last access: 18 August 2022.

McMurry, P. H., and Grosjean, D.: Gas and aerosol wall losses in Teflon film smog chambers, Environ. Sci. Technol., 19, 1176–1182, https://doi.org/10.1021/es00142a006, 1985.

Metzger, A., Dommen, J., Gaeggeler, K., Duplissy, J., Prevot, A. S. H., Kleffmann, J., Elshorbany, Y., Wisthaler, A., and Baltensperger, U.: Evaluation of 1,3,5 trimethylbenzene degradation in the detailed tropospheric chemistry mechanism, MCMv3.1, using environmental chamber data, Atmos. Chem. Phys., 8, 6453–6468, https://doi.org/10.5194/acp-8-6453-2008, 2008.

Ming, L., Jin, L., Li, J., Fu, P., Yang, W., Liu, D., Zhang, G., Wang, Z., and Li, X.: PM$_{2.5}$ in the Yangtze River Delta, China: Chemical compositions, seasonal variations, and regional pollution events, Environ. Pollut., 223, 200–212, https://doi.org/10.1016/j.envpol.2017.01.013, 2017.

Nakayama, T., Sato, K., Tsuge, M., Imamura, T., and Matsumi, Y.: Complex refractive index of secondary organic aerosol generated from isoprene/NO$_x$ photooxidation in the presence and absence of SO$_2$, J. Geophys. Res.-Atmos., 120, 7777–7787, https://doi.org/10.1002/2015jd023522, 2015.

Nakayama, T., Sato, K., Imamura, T., and Matsumi, Y.: Effect of Oxidation Process on Complex Refractive Index of Secondary Organic Aerosol Generated from Isoprene, Environ. Sci. Technol., 52, 2566–2574, https://doi.org/10.1021/acs.est.7b05852, 2018.

Ng, N. L., Kroll, J. H., Chan, A. W. H., Chhabra, P. S., Flagan, R. C., and Seinfeld, J. H.: Secondary organic aerosol formation from m-xylene, toluene, and benzene, Atmos. Chem. Phys., 7, 3909–3922, https://doi.org/10.5194/acp-7-3909-2007, 2007.

Qi, L., Liu, H., Shen, X., Fu, M., Huang, F., Man, H., Deng, F., Shaikh, A. A., Wang, X., Dong, R., Song, C., and He, K.: Intermediate-volatility organic compound emissions from nonroad construction machinery under different operation modes, Environ. Sci. Technol., 53, 13832–13840, https://doi.org/10.1021/acs.est.9b01316, 2019.

Qi, L., Zhao, J., Li, Q., Su, S., Lai, Y., Deng, F., Man, H., Wang, X., Shen, X., Lin, Y., Ding, Y., and Liu, H.: Primary organic gas emissions from gasoline vehicles in China: Factors, composition and trends, Environ. Pollut., 290, 117984, https://doi.org/10.1016/j.envpol.2021.117984, 2021.

Requia, W. J., Higgins, C. D., Adams, M. D., Mohamed, M., and Koutrakis, P.: The health impacts of weekday traffic: A health risk assessment of PM$_{2.5}$ emissions during congested periods, Environ. Int., 111, 164–176, https://doi.org/10.1016/j.envint.2017.11.025, 2018.

Santiago, M., Vivanco, M. G., and Stein, A. F.: SO$_2$ effect on secondary organic aerosol from a mixture of anthropogenic VOCs: experimental and modelled results, International J. Environ. Pollut., 50, 224–233, https://doi.org/10.1504/ijep.2012.051195, 2012.

Sato, K., Fujitani, Y., Inomata, S., Morino, Y., Tanabe, K., Hikida, T., Shimono, A., Takami, A., Fushimi, A., Kondo, Y., Imamura, T., Tanimoto, H., and Sugata, S.: A study of volatility by composition, heating, and dilution measurements of secondary organic aerosol from 1,3,5-trimethylbenzene, Atmos. Chem. Phys., 19, 14901–14915, https://doi.org/10.5194/acp-19-14901-2019, 2019.

Schauer, J. J., Kleeman, M. J., Cass, G. R., and Simoneit, B. R. T.: Measurement of emissions from air pollution sources. 5. C-1–C-32 organic compounds from gasoline-powered motor vehicles, Environ. Sci. Technol., 36, 1169–1180, https://doi.org/10.1021/es0108077, 2002.

Seinfeld, J. H. and Pandis, S. N.: Atmospheric chemistry and physics: from air pollution to climate change, in: 3rd Edn., John Wiley & Sons, Hoboken, ISBN 13: 978-1118947401, ISBN 10: 1118947401, 2016.

Sheehan, P. E. and Bowman, F. M.: Estimated effects of temperature on secondary organic aerosol concentrations, Environ. Sci. Technol., 35, 2129–2135, https://doi.org/10.1021/es001547g, 2001.

Shi, B., Wang, W., Zhou, L., Li, J., Wang, J., Chen, Y., Zhang, W., and Ge, M.: Kinetics and mechanisms of the gas-phase reactions of OH radicals with three C$_{15}$ alkanes, Atmos. Environ., 207, 75–81, https://doi.org/10.1016/j.atmosenv.2019.03.028, 2019a.

Shi, B., Wang, W., Zhou, L., Sun, Z., Fan, C., Chen, Y., Zhang, W., Qiao, Y., Qiao, Y., and Ge, M.: Atmospheric oxidation of C10–14 n-alkanes initiated by Cl atoms: Kinetics and mechanism, Atmos. Environ., 222, 117166, https://doi.org/10.1016/j.atmosenv.2019.117166, 2019b.

Sipila, M., Berndt, T., Petaja, T., Brus, D., Vanhanen, J., Stratmann, F., Patokoski, J., Mauldin, R. L., Hyvarinen, A. P., Lihavainen, H., and Kulmala, M.: The role of sulfuric acid in atmospheric nucleation, Science, 327, 1243–1246, https://doi.org/10.1126/science.1180315, 2010.

Sivaramakrishnan, R. and Michael, J. V.: Rate constants for OH with selected large alkanes: Shock-tube measurements and an improved group scheme, J. Phys. Chem. A, 113, 5047–5060, https://doi.org/10.1021/jp810987u, 2009.

Srivastava, D., Vu, T. V., Tong, S., Shi, Z., and Harrison, R. M.: Formation of secondary organic aerosols from anthropogenic precursors in laboratory studies, npj Clim. Atmos. Sci., 5, 22, https://doi.org/10.1038/s41612-022-00238-6, 2022.

Takekawa, H., Minoura, H., and Yamazaki, S.: Temperature dependence of secondary organic aerosol formation by photooxidation of hydrocarbons, Atmos. Environ., 37, 3413–3424, https://doi.org/10.1016/s1352-2310(03)00359-5, 2003.

Tsai, S. S., Chang, C. C., and Yang, C. Y.: Fine particulate air pollution and hospital admissions for chronic obstructive pulmonary disease: a case-crossover study in Taipei, Int. J. Environ. Res. Publ. Health, 10, 6015–6026, https://doi.org/10.3390/ijerph10116015, 2013.

Tsiligiannis, E., Hammes, J., Salvador, C. M., Mentel, T. F., and Hallquist, M.: Effect of NO$_x$ on 1,3,5-trimethylbenzene (TMB) oxidation product distribution and particle formation, Atmos. Chem. Phys., 19, 15073–15086, https://doi.org/10.5194/acp-19-15073-2019, 2019.

Wall, K. J. and Harris, G. W.: Uptake of nitrogen dioxide (NO$_2$) on acidic aqueous humic acid (HA) solutions as a missing daytime nitrous acid (HONO) surface source, J. Atmos. Chem., 74, 283–321, https://doi.org/10.1007/s10874-016-9342-8, 2016.

Wang, C., Yuan, B., Wu, C., Wang, S., Qi, J., Wang, B., Wang, Z., Hu, W., Chen, W., Ye, C., Wang, W., Sun, Y., Wang, C., Huang, S., Song, W., Wang, X., Yang, S., Zhang, S., Xu, W., Ma, N., Zhang, Z., Jiang, B., Su, H., Cheng, Y., Wang, X., and Shao, M.: Measurements of higher alkanes using NO$^+$ chemical ionization in PTR-ToF-MS: important contributions of higher alkanes to secondary organic aerosols in China, Atmos. Chem. Phys., 20, 14123–14138, https://doi.org/10.5194/acp-20-14123-2020, 2020.

Wang, S., Du, L., Tsona, N. T., Jiang, X., You, B., Xu, L., Yang, Z., and Wang, W.: Effect of NO$_x$ and SO$_2$ on the photooxidation of methylglyoxal: Implications in secondary aerosol formation, J. Environ. Sci., 92, 151–162, https://doi.org/10.1016/j.jes.2020.02.011, 2020.

Wang, W. G., Liu, M. Y., Wang, T. T., Song, Y., Zhou, L., Cao, J. J., Hu, J. N., Tang, G. G., Chen, Z., Li, Z. J., Xu, Z. Y., Peng, C., Lian, C. F., Chen, Y., Pan, Y. P., Zhang, Y. H., Sun, Y. L., Li, W. J., Zhu, T., Tian, H. Z., and Ge, M. F.: Sulfate formation is dominated by manganese-catalyzed oxidation of SO$_2$ on aerosol surfaces during haze events, Nat. Commun., 12, 10, https://doi.org/10.1038/s41467-021-22091-6, 2021.

Wang, Y., Wang, Y., Wang, L., Petäjä, T., Zha, Q., Gong, C., Li, S., Pan, Y., Hu, B., Xin, J., and Kulmala, M.: Increased inorganic aerosol fraction contributes to air pollution and haze in China, Atmos. Chem. Phys., 19, 5881–5888, https://doi.org/10.5194/acp-19-5881-2019, 2019.

Warren, B., Austin, R. L., and Cocker, D. R.: Temperature dependence of secondary organic aerosol, Atmos. Environ., 43, 3548–3555, https://doi.org/10.1016/j.atmosenv.2009.04.011, 2009.

Wu, L. Y., Tong, S. R., Zhou, L., Wang, W. G., and Ge, M. F.: Synergistic effects between SO$_2$ and HCOOH on alpha-Fe$_2$O$_3$, J. Phys. Chem. A, 117, 3972–3979, https://doi.org/10.1021/jp400195f, 2013.

Xu, R., Alam, M. S., Stark, C., and Harrison, R. M.: Composition and emission factors of traffic- emitted intermediate volatility and semi-volatile hydrocarbons (C$_{10}$–C$_{36}$) at a street canyon and urban background sites in central London, UK, Atmos. Environ., 231, 117448, https://doi.org/10.1016/j.atmosenv.2020.117448, 2020.

Yang, Z., Tsona, N. T., Li, J., Wang, S., Xu, L., You, B., and Du, L.: Effects of NO$_x$ and SO$_2$ on the secondary organic aerosol formation from the photooxidation of 1,3,5-trimethylbenzene: A new source of organosulfates, Environ. Pollut., 264, 114742, https://doi.org/10.1016/j.envpol.2020.114742, 2020.

Yee, L. D., Craven, J. S., Loza, C. L., Schilling, K. A., Ng, N. L., Canagaratna, M. R., Ziemann, P. J., Flagan, R. C., and Seinfeld, J. H.: Effect of chemical structure on secondary organic aerosol formation from C$_{12}$ alkanes, Atmos. Chem. Phys., 13, 11121–11140, https://doi.org/10.5194/acp-13-11121-2013, 2013.

Zhang, Q., Zheng, Y., Tong, D., Shao, M., Wang, S., Zhang, Y., Xu, X., Wang, J., He, H., Liu, W., Ding, Y., Lei, Y., Li, J., Wang, Z., Zhang, X., Wang, Y., Cheng, J., Liu, Y., Shi, Q., Yan, L., Geng, G., Hong, C., Li, M., Liu, F., Zheng, B., Cao, J., Ding, A., Gao, J., Fu, Q., Huo, J., Liu, B., Liu, Z., Yang, F., He, K., and Hao, J.: Drivers of improved PM$_{2.5}$ air quality in China from 2013 to 2017, P. Natl. Acad. Sci. USA, 116, 24463–24469, https://doi.org/10.1073/pnas.1907956116, 2019.

Zhang, W., Wang, W., Li, J., Peng, C., Li, K., Zhou, L., Shi, B., Chen, Y., Liu, M., and Ge, M.: Effects of SO$_2$ on optical properties of secondary organic aerosol generated from photooxidation of toluene under different relative humidity, Atmos. Chem. Phys. 20, 4477–4492, https://doi.org/10.5194/acp-20-4477-2020, 2020.

Zhang, X., Cappa, C. D., Jathar, S. H., McVay, R. C., Ensberg, J. J., Kleeman, M. J., and Seinfeld, J. H.: Influence of vapor wall loss in laboratory chambers on yields of secondary organic aerosol, P. Natl. Acad. Sci. USA, 111, 5802–5807, 2014.